

# Characterisation of wake-region optical emissions from an ablative hypersonic glide vehicle



Jarrad M. Knight\* and Jordan A.C. Kildare†

*University of South Australia, Adelaide, South Australia, 5095, Australia*

Fabian Zander‡

*University of Southern Queensland, Toowoomba, Queensland, 4350, Australia*

Yee Wei Law§ and Michael J. Evans¶

*University of South Australia, Adelaide, South Australia, 5095, Australia*

**The effect of ablation on the structure and chemical composition of the wake behind the HIFIRe-5 vehicle at Mach 12.6 and 30 km altitude is examined to enhance understanding of possible wake-region emission spectra. A coupled flow-radiation-ablation numerical model is developed to resolve wake-region translational and vibro-electronic temperatures and the number densities of both air and ablation-derived species. For an ablating vehicle, carbon monoxide (CO) and carbon dioxide (CO<sub>2</sub>) are identified as the major ablation products entering the wake, while wake-region nitric oxide (NO) is also enhanced relative to the non-ablating vehicle. The developed wake exhibits two apparent neck positions, driven by forebody boundary-layer crossflow, producing localized peaks in translational and vibro-electronic temperatures in the wake.**

## I. Nomenclature

$A_f$	= pre-exponential factor, $\text{m}^3 \cdot \text{kmol}^{-1} \cdot \text{s}^{-1}$
$C'_H$	= modified heat transfer coefficient, $\text{kg} \cdot \text{m}^{-2} \cdot \text{s}^{-1}$
$C_H$	= heat transfer coefficient, $\text{kg} \cdot \text{m}^{-2} \cdot \text{s}^{-1}$
$C_M$	= mass transfer coefficient, $\text{kg} \cdot \text{m}^{-2} \cdot \text{s}^{-1}$
$h_w$	= wall enthalpy, $\text{J} \cdot \text{kg}^{-1}$
$Ma$	= mach Number
$M$	= molecular weight, $\text{kg} \cdot \text{mol}^{-1}$
$R$	= universal gas constant, $\text{J} \cdot \text{mol}^{-1} \cdot \text{K}^{-1}$
$Re'$	= freestream unit Reynolds number, $\text{m}^{-1}$
$T_f$	= characteristic temperature of reaction
$T_t$	= translational Temperature, K
$T_{ve}$	= vibro-electronic Temperature, K
$T_x$	= control temperature of reaction
$Y$	= mass fraction
$\beta$	= pre-exponential temperature exponent
$\gamma$	= reaction efficiency
$\lambda$	= blowing correction factor
$\phi$	= body-fixed angular coordinate around vehicle circumference, °
$\rho$	= density, $\text{kg} \cdot \text{m}^{-3}$
$\dot{m}_c$	= mass-flow rate of char gas, $\text{kg} \cdot \text{m}^{-2} \cdot \text{s}^{-1}$

\*PhD Candidate, UniSA STEM

†Research Fellow, UniSA STEM, AIAA Member

‡Associate Professor, School of Engineering, AIAA Senior Member

§Senior Lecturer, UniSA STEM

¶Senior Lecture, UniSA STEM, AIAA Senior Member

## II. Introduction

A hypersonic glide vehicle (HGV) is a type of vehicle which can maneuver and glide through the atmosphere at hypersonic speeds, typically defined as over five times the local speed of sound. The high enthalpy conditions experienced by these vehicles has led to the consideration of material ablation as means of protecting vehicle structural integrity and alleviating high heat flux [1]. These materials, which are typically carbon-based [2], can be described as a sacrificial material which erodes under high temperature and pressure conditions through processes such as surface oxidation, nitridation, and direct sublimation. The chemical products formed from ablation has been shown to substantially increase shock-layer and wake luminosity [3–5]. These products include, but are not limited to: carbon dioxide ( $\text{CO}_2$ ), carbon monoxide (CO), and diatomic carbon ( $\text{C}_2$ ).  $\text{CO}_2$  is known to radiate strongly in the infrared at approximately 2700nm and 4300nm [6, 7], while CO has various emission bands which are strongest in the near-ultraviolet (95–382nm) and span to visible-near infrared band systems (390–859nm) [8–10]. In the absence of ablation products, a wake comprised of dissociated and ionised air exhibits a different optical signature [4], dominated by emission features from molecular nitrogen ( $\text{N}_2$ ), molecular oxygen ( $\text{O}_2$ ), and nitric oxide (NO) [11]. Emissions from  $\text{N}_2$ ,  $\text{O}_2$ , and ultraviolet bands from NO may be partially reabsorbed by surrounding species, particularly in regions with elevated ozone concentrations, which can reduce their apparent emission intensity [12, 13].

Although individual emission features from hypersonic bodies are well-known, the complete emission spectra is less certain. Numerically predicting emission spectra generally requires a line-by-line radiation code, which requires spatially resolved thermal and species distributions. Such distributions have been particularly well-characterized for the wake developed by a non-ablating blunt-body re-entry vehicle using computational fluid dynamics (CFD) [14–19]. The HGV, however, produces a different wake structure [20] due to its sustained near-horizontal glide trajectory [21], shown schematically in Figure 1.

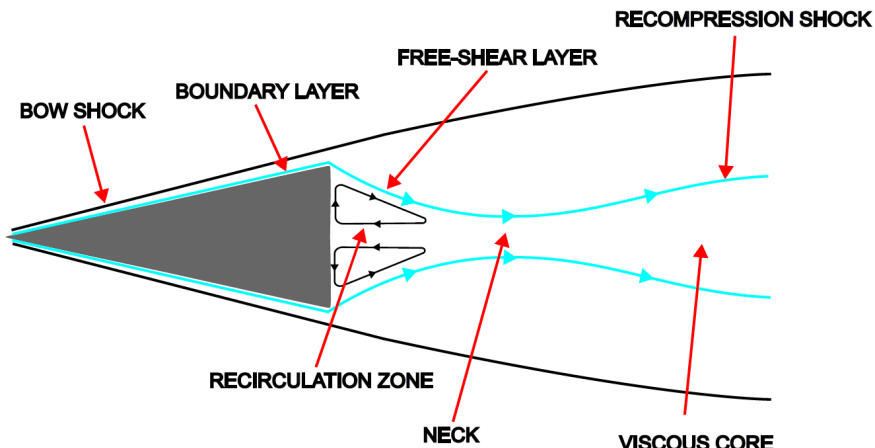


Fig. 1 Schematic of near-wake flowfield for slender hypersonic body.

Boundary-layer separation from a slender hypersonic body results in a thin shear-layer, enclosing a backward-flowing, subsonic recirculation region. Further downstream, the separated shear-layers contract to form a high-temperature, neck-stagnation point, where flow velocity may theoretically reach zero [22]. Downstream of the neck, flow expands producing a recompression shock, enclosing a viscous wake core. Across the entire wake, the high temperature gas typically remains in a state of thermochemical nonequilibrium, a condition which strongly influences emission features [22]. The introduction of ablation products into the wake region is expected to alter the wake structure and thermochemical composition, which may alter observability [4, 23].

Ablation in hypersonic environments has been widely studied, with extensive literature addressing material response and shock-layer radiation [24–30]. Comparatively little attention has been brought to how ablation products spatially evolve within the wake region. The structural and chemical composition of the wake behind a Mach 7, axisymmetric sphere-cone using an AVCOAT ablative heat shield material was reported by [31]. AVCOAT is comprised of silica fibers in an epoxy novolac resin and is typically used in reentry environments [32], and may not be representative of the thermal protection systems used for glide vehicles. Furthermore, demonstrated glide vehicles such as HTV-2 [33] and HiFiRE-5 [34] are non-axisymmetric, implying a different wake structure. To investigate the effect of ablation on the wake generated by a non-axisymmetric HGV, this study computes and analyses the thermochemical environment of a

generic, non-axisymmetric hypersonic vehicle at Mach 11 and 30km altitude.

### III. Computational model and methodology

#### A. Flowfield Modelling

A modified version of the open-source transient CFD code hy2Foam [35] is used in this work, based on the OpenFOAM-v1706 framework. The solver includes detailed models for thermochemical nonequilibrium and species transport, which are reviewed in [36, 37]. The solver has been extended in this work to be loosely coupled with a discrete-ordinates radiation model which enables application of a radiation-convection-ablation equilibrium boundary condition, which is discussed in Subsection III.C. In this work, the following nineteen species are considered: N, N<sup>+</sup>, N<sub>2</sub>, N<sub>2</sub><sup>+</sup>, O, O<sup>+</sup>, O<sub>2</sub>, O<sub>2</sub><sup>+</sup>, NO, NO<sup>+</sup>, e<sup>-</sup>, C, C<sup>+</sup>, C<sub>2</sub>, CO, CO<sup>+</sup>, CN, CN<sup>+</sup>, CO<sub>2</sub>. Transport properties for these species are taken from Ref. [38, 39], the chemical reaction rates for all species involving air are taken from [40], with additional third-body efficiencies from [25]. Chemical reaction rates for species involving carbon are based on Refs. [25, 26, 41–43] and are detailed in Table 2.

**Table 2 Reaction kinetics for ablation species in the present model. Rates are computed using the modified Arrhenius equation [42].**

i	Reaction	A <sub>f,i</sub> , m <sup>3</sup> · kmol · s <sup>-1</sup>	β <sub>i</sub>	T <sub>f,a</sub> , K	T <sub>x</sub>	Third Body, M	Ref
1	CO <sub>2</sub> + M ⇌ CO + O + M	1.38e+19	-1.50	6.328e+4	T <sub>a</sub>	N,C,O	[26]
2		6.90e+18	-1.50	6.328e+4	T <sub>a</sub>	Others	[26]
3	CO + M ⇌ C + O + M	1.80e+18	-1.00	1.290e+5	T <sub>a</sub>	N,C,O	[26]
4		1.20e+18	-1.00	1.290e+5	T <sub>a</sub>	Others	[26]
5	C <sub>2</sub> + M ⇌ 2 C + M	4.50e+15	-1.00	7.150e+4	T <sub>a</sub>	All	[26]
6	CN + M ⇌ C + N + M	6.00e+12	-0.40	7.100e+4	T <sub>a</sub>	All	[41]
7	CO + O ⇌ C + O <sub>2</sub>	3.90e+10	-0.18	6.920e+4	T <sub>t</sub>		[42]
8	CO + N ⇌ CN + O	1.00e+12	0.00	6.860e+4	T <sub>t</sub>		[26]
9	CO + N ⇌ C + NO	1.10e+11	0.07	5.350e+4	T <sub>t</sub>		[26]
10	CO + NO ⇌ CO <sub>2</sub> + N	3.00e+03	0.88	1.330e+4	T <sub>t</sub>		[41]
11	CO + N <sub>2</sub> ⇌ CN + NO	1.20e+13	-1.23	7.700e+4	T <sub>t</sub>		[41]
12	CO + C ⇌ C <sub>2</sub> + O	2.00e+14	-1.00	5.800e+4	T <sub>t</sub>		[42]
13	CN + O ⇌ NO + C	1.00e+12	0.00	3.860e+4	T <sub>t</sub>		[42]
14	CN + C ⇌ C <sub>2</sub> + N	3.00e+11	0.00	1.810e+4	T <sub>t</sub>		[41]
15	C + N <sub>2</sub> ⇌ CN + N	1.10e+11	-0.11	2.320e+4	T <sub>t</sub>		[42]
16	C <sub>2</sub> + N <sub>2</sub> ⇌ 2 CN	1.50e+10	0.07	2.100e+4	T <sub>t</sub>		[43]
17	CO <sub>2</sub> + O ⇌ O <sub>2</sub> + CO	2.71e+11	0.00	3.380e+4	T <sub>t</sub>		[25]
18	C + O ⇌ CO <sup>+</sup> + e <sup>-</sup>	8.80e+05	1.00	3.310e+4	T <sub>t</sub>		[42]
19	C + N ⇌ CN <sup>+</sup> + e <sup>-</sup>	1.00e+12	1.50	1.644e+5	T <sub>t</sub>		[43]
20	C + NO <sup>+</sup> ⇌ C <sup>+</sup> + NO	1.00e+10	0.00	2.320e+04	T <sub>t</sub>		[42]
21	C + e <sup>-</sup> ⇌ C <sup>+</sup> + 2 e <sup>-</sup>	3.90e+30	-3.78	1.307e+05	T <sub>ve</sub>		[42]
22	C <sup>+</sup> + CO ⇌ C + CO <sup>+</sup>	1.00e+10	0.00	3.140e+04	T <sub>t</sub>		[42]
23	C <sup>+</sup> + O <sub>2</sub> ⇌ C + O <sub>2</sub> <sup>+</sup>	1.00e+10	0.00	9.400e+03	T <sub>t</sub>		[42]

To improve numerical stability, a modified temperature formulation (Eq. (1)) is introduced into reaction rate calculations to prevent non-physical backward reaction rates in low-temperature regions [44]:

$$T' = \frac{1}{2} \left( (T + T_{\min}) + \sqrt{(T - T_{\min})^2 + \epsilon^2} \right) \quad (1)$$

where  $T$  is the original temperature of the field,  $T_{min}$  is the minimum allowable temperature, and  $\epsilon$  is a smoothing parameter. In this work  $T_{min}$  is set to 500 K and  $\epsilon = 50K$  across the forebody and in the wake for each case. A maximum Courant number of 0.2 is employed across the wake and forebody, with second-order numerical solution schemes with the exception of a first-order time-stepping scheme to achieve steady-state results.

## B. Finite-Rate Surface Chemistry Model

Carbonaceous materials exposed to high-temperature air may undergo complex physicochemical reactions, including oxidation, nitridation, sublimation, and diffusion. Sublimation typically begins at temperatures of 3000–4000K [45, 46], which is well above the predicted peak wall stagnation temperatures in this study, and is therefore not considered. For oxidation and nitridation of carbon, the following reactions are possible [25, 47–49]:



The forward reaction rate,  $k_f$  for each reaction above can be written as [48]:

$$k_{f,i} = \gamma_i \sqrt{\frac{RT}{2\pi M_i}} \quad (5)$$

where  $\gamma$  is the reaction efficiency between the surface and reactant  $i$ ,  $T$  is the temperature of the wall, and  $M_i$  is the molar mass of the reactant in kg·mol<sup>-1</sup>, the reaction efficiency for each reaction is shown in Table 3

**Table 3 Reaction efficiency for oxidation and nitridation of carbon**

Reaction	Probability, $\gamma$	Ref.
$C_{(s)} + O_{(g)} \longrightarrow CO_{(g)}$	$0.63e^{(-1160/T)}$	[48]
$2 C_{(s)} + O_{2(g)} \longrightarrow 2 CO_{(g)}$	$\frac{1.43 \times 10^{-3} + 0.01e^{-1450/T}}{1 + 2.0 \times 10^{-4}e^{13000/T}}$	[48]
$C_{(s)} + N_{(g)} \longrightarrow CN_{(g)}$	0.01	[50]

## C. Ablation Modelling

The solver hy2Foam has also been extended to be fully-coupled with a one-dimensional ablation model, based on implementations from the OpenFOAM codes PATO [51] and FireFOAM [52, 53], which have both been validated for ablation of carbon-based composites [51, 54]. For equilibrium ablation, assuming that Prandtl and Lewis numbers are equal to unity and the diffusion coefficients are identical between elements, the mass balance at the wall of a non-pyrolyzing ablator may be written as [51]:

$$C'_H (Y_{i,w} - Y_{i,e}) + \dot{m}_c Y_{i,w} = \dot{m}_c Y_{i,c} \quad (6)$$

where  $Y_i$  is the mass fraction of species  $i$  evaluated at the wall ( $w$ ), at the boundary-layer edge ( $e$ ), and in the char layer ( $c$ ). The modified convective coefficient  $C'_H$  accounts for blockage induced by the blowing of ablation gas, and is given by the blowing correction [55] :

$$C'_H = C_H \frac{\ln(1 + 2\lambda(\dot{m}_c/C_M))}{2\lambda(\dot{m}_c/C_M)}, \quad (7)$$

where  $C_H$  is the heat transfer coefficient and is calculated from the Stanton number for heat transfer,  $\lambda$  is a blowing correction factor and is taken equal to 0.5, based on recommendations from Ref. [55].  $C_M$  is the mass transfer coefficient which is calculated from the Stanton number for mass transfer.

The wall temperature  $T_w$  is computed with an equilibrium surface energy balance model, which assumes that the inwards convective and radiative heat from the gas are equal to the outward radiative and advective heat from char gas.

$$q_{conv} + q_{rad}^{in} = \varepsilon_w \sigma (T_w^4 - T_\infty^4) + \dot{m}_c h_w \quad (8)$$

where  $h_w$  is the wall enthalpy,  $\varepsilon_w$  is the emissivity of the carbon surface and is set to be 0.8 [56],  $\sigma$  is the Stefan-Boltzmann constant. The convective radiative flux  $q_{conv}$  is evaluated using correlations for the average Nusselt number across a flat-plate and  $q_{rad}$  is evaluated using a discrete-ordinates radiation model.

#### D. Vehicle Description and Coordinate System

The HIFiRE-5 flight vehicle, shown schematically in Figure 2, is chosen as the representative geometry for this work, as it is a well-documented vehicle with associated test-flight data [34, 61–63]. The design and dimensions of the vehicle are explained in Ref. [64]. In this work, the XY and ZX planes of the vehicle are defined as the vehicle's pitch and yaw planes, respectively, and the body-fixed angular coordinate  $\phi$  is measured around the vehicle's roll axis, with  $\phi = 0^\circ$  at the centerline and  $\phi = 90^\circ$  at the leading edge.

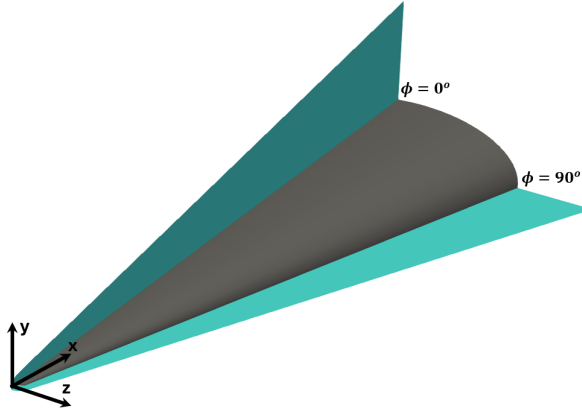


**Fig. 2 HIFiRE-5 geometry and coordinate system. Flow is in the x-direction.**

#### E. Model Validation

##### 1. Double cone experiment

A double cone configuration subject to hypersonic flow conditions displays intricate flow features, including shock-shock and shock-boundary layer interactions. Accurate simulation of the flow field under such conditions poses significant challenges to CFD codes [57] and therefore provides a good metric to assess the validity of most numeric codes [58]. Experimental conditions acquired from Ref. [59] for nitrogen flow around a double cone configuration with semi-angles of  $25^\circ$  and  $55^\circ$  and a base diameter of 10.3 inches is shown below in Table 4, where conditions are taken from Run 40 of the experiment.

**Table 4 Double cone experimental conditions : Run 40 [59]**

Mach Number, Ma	Velocity, km/s	$T_\infty$ , K	$p_\infty$ , Pa	$Re'$ , $\cdot 10^6 \cdot m^{-1}$
11.72	3.094	173.0	129.0	0.690

An axisymmetric structured grid was constructed with a clustered number of cells normal to the surface of the wall, becoming sparser further from regions of weak viscous-inviscid interaction. Figure 3 shows comparisons between calculated and experimental results for the static wall pressure and heat flux along the double-cone surface.

Good agreement is found between the code and experiment for the overall trend of wall pressure and heat flux. This suggests inviscid shock interactions along the surface are resolved. The recorded secondary peak in heat flux centered around  $x = 0.13$  appears to be predicted further upstream by the model as compared to the experiment. These observations indicate the code may not be well-suited to conditions where small-scale flow features dominate, however given the primary interest of this study is the broader flow over this vehicle and into the wake, these localized discrepancies can be considered less critical.

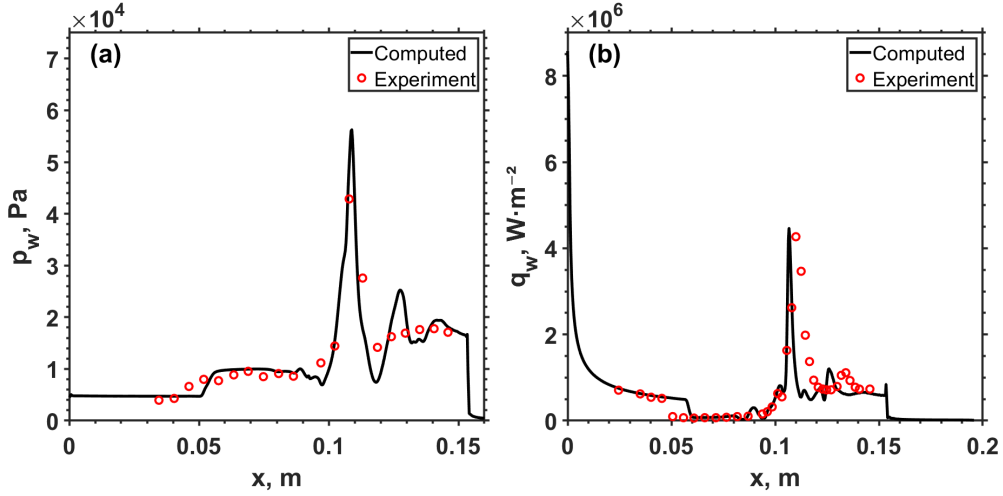


**Fig. 3** Comparison of computed and experimental surface conditions from Run 40 [59] on the double cone. (a) Static wall pressure,  $p_w$ ; (b) Wall heat flux,  $q_w$

## 2. HIFiRE-5b

Flight conditions from the HIFiRE-5b experiment at 512 s after launch are used to verify the radiative-equilibrium thermal boundary condition for the geometry shown in Figure 4. The relevant conditions are listed in Table 5.

**Table 5** HIFiRE-5b flight conditions at 512 s after launch [60]

Time, s	Mach Number, Ma	$Re', 10^6 \cdot \text{m}^{-1}$
512	7.65	3.34

Figure 4 shows the surface temperature predictions from the code compared to flight data [34], where  $\phi$  refers to the body-fixed angular coordinate around the vehicle's roll axis. Excellent agreement is seen along the leading edge of the vehicle and the overall trend is captured along the stagnation line, being under-predicted by no greater than 40 K. Available thermocouple data from the HIFiRE-5b experiment is limited to  $0.2 < x < 0.8$  [34], so direct comparison is not possible closer to the nose. Nevertheless, the agreement seen along the leading edge and stagnation line suggests that predictions remain reliable upstream of  $x > 0.2$ .

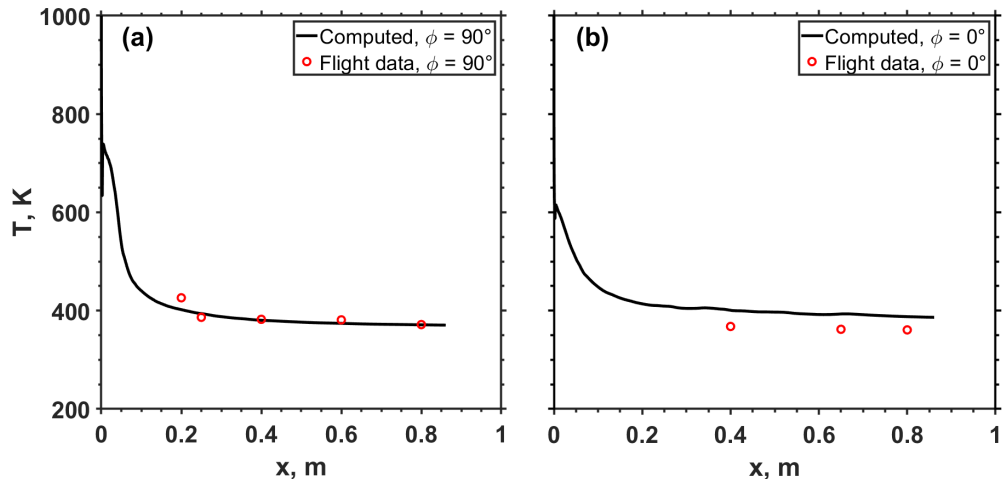


**Fig. 4** Comparison of predicted surface temperature and in-flight surface temperature of the HIFiRE-5b flight vehicle at 512 seconds. (a) Vehicle leading edge,  $\phi = 90^\circ$ ; (b) Vehicle centerline,  $\phi = 0^\circ$

## F. Simulation Methodology

The HIFiRE-5 vehicle is simulated at 30 km altitude, with a flight speed taken from a generic flight profile reported by [65], the flight details are provided in Table 6. The altitude and speed was selected to ensure laminar flow over the vehicle within simulations, guided by transition data reported by [61].

**Table 6 Flight conditions used in this work**

Mach Number, Ma	Altitude, km	Velocity, $\text{km}\cdot\text{s}^{-1}$	$T_\infty, \text{K}$	$\rho_\infty, \cdot 10^{-3} \cdot \text{kg} \cdot \text{m}^{-3}$	$\text{Re}', 10^6 \cdot \text{m}^{-1}$
12.6	30.0	3.80	227	18.4	4.74

Steady state results from forebody simulations were used to provide an inflow boundary condition into the wake domain. In both the forebody and wake domains, symmetry plane boundary conditions are imposed on both the XY and ZX planes to exploit the geometric symmetry of the HIFiRE-5 vehicle and zero angle-of-attack assumption. Across the forebody, cells are clustered normal to the wall with a constant normal growth rate of 1.05 to resolve the boundary layer and capture shock structures. In the wake domain, the grid was generated to produce cells with an approximate aspect ratio of unity up to the expected wake neck, which was determined from initial coarse simulations. The wake domain is sized to 1.0m (1.16 body lengths) to ensure the domain remains laminar, based on reported wake transition data from Ref. [66]. A mesh independence study revealed a forebody grid and wake grid with cell count of approximately 650K and 9.33M cells, respectively, were sufficient to capture relevant flow structures.

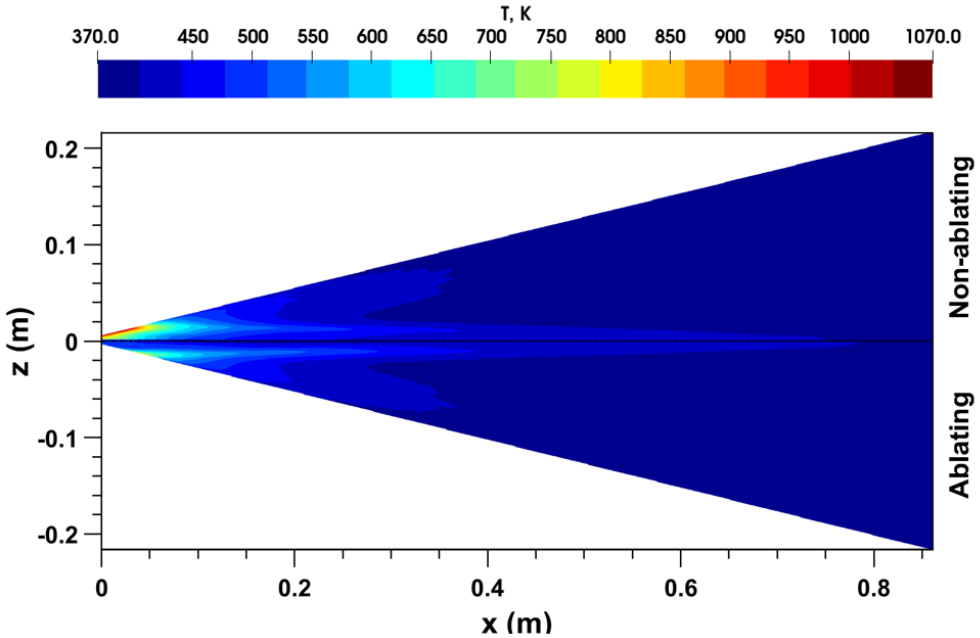
## IV. Results and Discussion

### A. Forebody

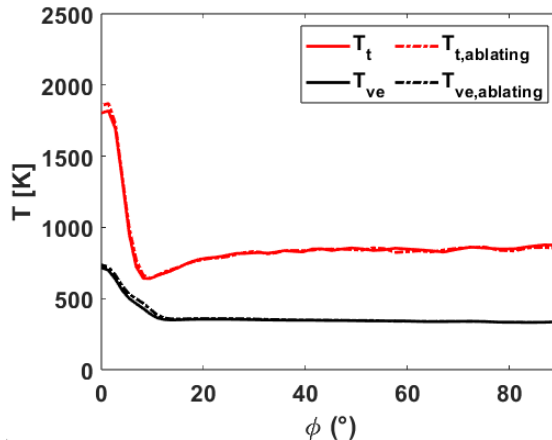
Figure 5 shows a top-down view of the computed wall temperature downstream of the nose under ablating and non-ablating conditions. The peak temperature along the body for the non-ablating case is approximately 1070 K, while for the ablating case it is lower at 674 K. Off-centerline hot streaks are observed for the non-ablating case. These are formed from boundary-layer deflection from the leading-edge towards the vehicle centerline, which allows a thickened boundary-layer near the vehicle centerline and therefore reduced heating [67]. This flow feature was first observed in experiments from Ref. [68] and in many subsequent numerical work [67, 69–71]. Under ablating conditions, the same deflection pattern persists, with off-centerline hot streaks forming at similar locations. However, the temperature along the centerline and near the leading edge is noticeably reduced compared to the non-ablating case. This reduction is consistent with blowing-induced thickening of the boundary-layer, caused by the injection of CO and CN into the flow. The added mass flux weakens near-wall convective heat-transfer, suppressing peak heating that appears in the non-ablating case.

Figure 6 shows the computed translational ( $T_t$ ) and vibro-electronic ( $T_{ve}$ ) temperature of gas across the aft-section of the vehicle. Negligible difference can be seen in temperature along the circumference of the vehicle under ablating and non-ablating conditions, which suggests the ablation rates are insufficient to change downstream flow structure. Near the vehicle centerline ( $\phi = 0^\circ$ ),  $T_t$  and  $T_{ve}$  are 1818 K and 717 K respectively for the non-ablating case, while for the ablating case  $T_t$  and  $T_{ve}$  are 1872 K and 736 K respectively. For  $\phi > 4^\circ$ , the  $T_t$  profiles converge for both cases, and for  $\phi > 30^\circ$   $T_{ve}$  the profiles likewise become indistinguishable. The high temperature region formed along the centerline can again be explained through deflection of the boundary-layer from the leading-edge towards the centerline, allowing a high-temperature, mushroom-like thermal structure [67].

Figure 7 shows the computed number density of air and ablation species along the aft-section of the vehicle. Under ablating conditions, more NO, N, and O are found to enter the wake from within the boundary-layer. The production of nitric oxide (NO) under ablating conditions may be increased through reactions 9, 11 and 13 from Table 2. For ablation species, the only species found to exist at appreciable quantity along the aft-section of the vehicle are CO and CO<sub>2</sub>. Relative to other species formed from ablation, CO is at greatest concentration across the aft-section, owing to the high surface reactivity of atomic oxygen at the vehicle surface. Alongside CO, notable quantities of CO<sub>2</sub> are also found along the aft-section of the vehicle. In the present model, CO<sub>2</sub> can be produced through several reactions listed in Table 2, that remain active within the high-temperature boundary-layer (Figure 6). Reaction 10 (CO + NO  $\rightleftharpoons$  CO<sub>2</sub> + N) provides a direct route for CO oxidation, and the combination of CO and elevated NO in the flow produces the appreciable CO<sub>2</sub> observed along the body.



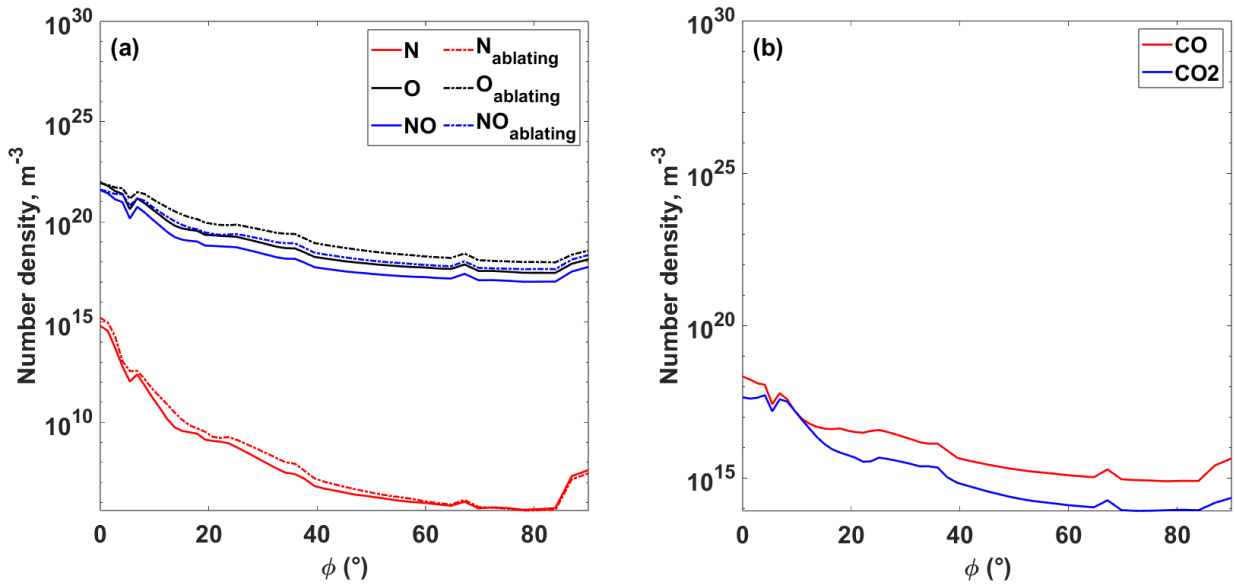
**Fig. 5** Top-down view of computed wall temperature, K.  $z > 0$ : Non-ablating;  $z < 0$  : Ablating



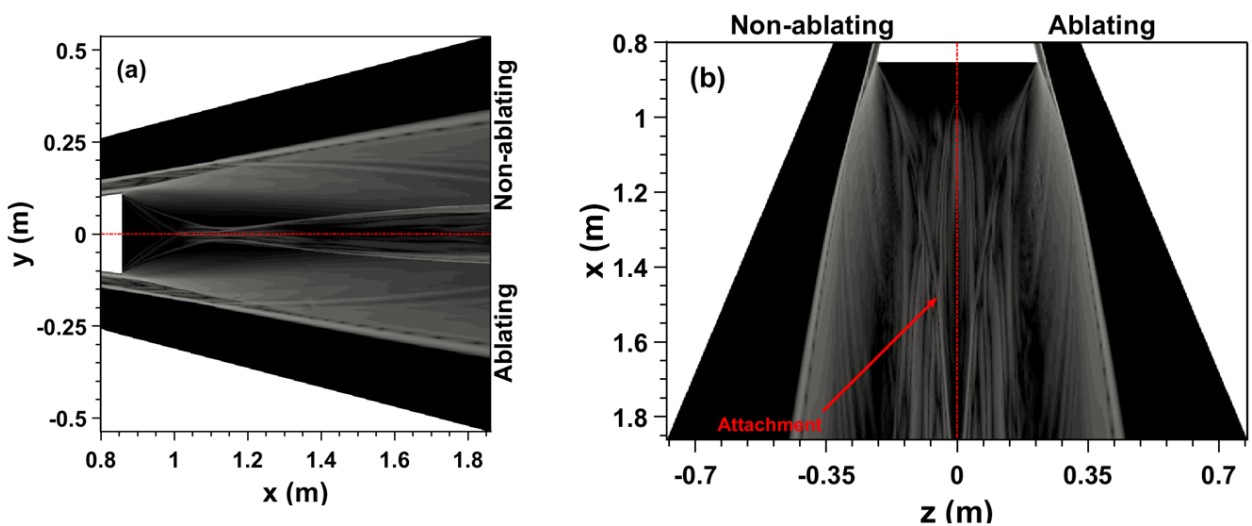
**Fig. 6** Aft-end gaseous  $T_t$  and  $T_{ve}$ , K, along edge of vehicle.  $\phi = 0^\circ$  at centerline and  $\phi = 90^\circ$  at leading edge. Solid line: Non-ablating. Dashed line: Ablating

## B. Wake region

Figure 8 shows the computed absolute density gradient,  $|\nabla\rho|$ , of the flowfield under ablating and non-ablating conditions. Negligible differences can be seen in the field between both conditions, with no difference in neck, shear-layer and wake core structure. This suggests the recorded ablation rates were insufficient to impact flow structure. Across both cases, thin, strong density gradients are observed through shear layers in the XY plane and through shock boundaries developed in both the XY and ZX planes, consistent with [22]. Weaker shear-layers developed in the ZX plane can be seen intersecting the wake shock, as annotated in Figure 8b. This leads to recompression of the viscous core downstream of the attachment point, producing a complex wake structure where there are two apparent neck positions.



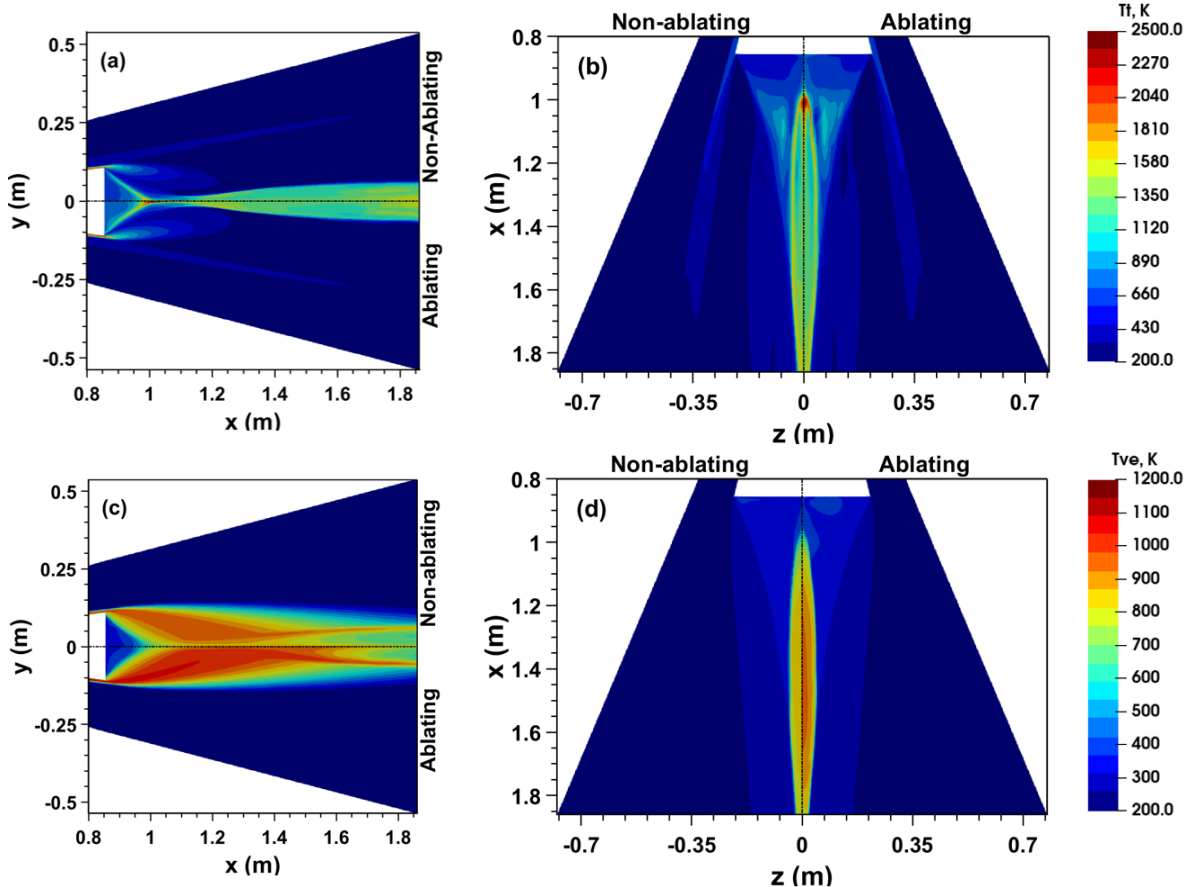
**Fig. 7** Wall-normal number densities,  $\text{m}^{-3}$ , of species along aft-section of vehicle.  $\phi = 0^\circ$  at centerline and  $\phi = 90^\circ$  at leading edge. (a) N, O, NO under ablating conditions (dashed line) and non-ablating conditions (solid line); (b) CO, CO<sub>2</sub>



**Fig. 8** Planar sections of density-gradient,  $|\nabla \rho|$ , under ablating and non-ablating conditions. (a)  $|\nabla \rho|$  in XY plane, non-ablating  $y > 0$ , ablating  $y < 0$ ; (b)  $|\nabla \rho|$  in ZX plane, non-ablating  $z < 0$ , ablating  $z > 0$

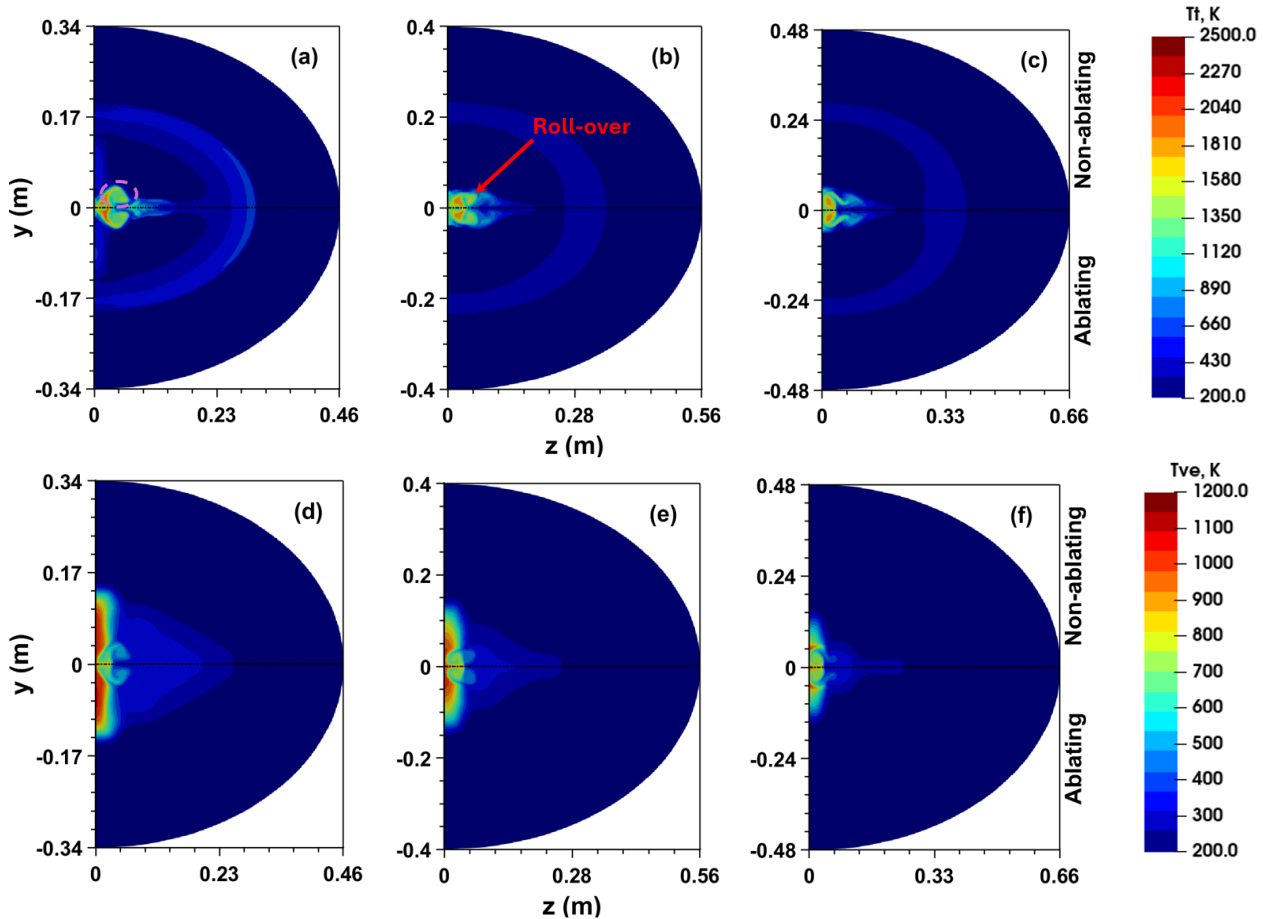
Figure 9 shows the translational ( $T_t$ ) and vibro-electronic ( $T_{ve}$ ) temperatures of the wake under ablating and non-ablating conditions in both the XY and ZX planes. Under ablating conditions,  $T_t$  reaches a peak of a maximum 2470 K at the wake neck in the XY plane, while  $T_{ve}$  reaches a maximum of 1080 K in the expansion region of the XY plane. For non-ablating conditions, both  $T_t$  and  $T_{ve}$  peak at the same locations, with a maximum  $T_t$  of 2290 K and maximum  $T_{ve}$  of 990 K. The elevated  $T_{ve}$  in the ablating case reflects the transport of vibrationally excited ablation products into the wake, which carry energy in their vibrational and electronic modes which relax slower than translational energy [22].

Across both conditions in Figure 9, regions of high  $T_t$  are observed at the wake neck and along the boundaries of the wake shock, consistent with classical hypersonic wake behavior [22]. Regions of high  $T_{ve}$  appear in the expansion region and along the boundaries of the recompression shock in the XY plane. In the ZX plane,  $T_{ve}$  also peaks throughout the wake core due to shear layer reattachment (Figure 8b), which compresses the wake core and induces downstream heating near  $x = 1.5$ . This recompression increases  $T_t$  by approximately 200 K and  $T_{ve}$  by a similar amount under both conditions.



**Fig. 9** Temperature profiles, K, in the wake for ablating and non-ablating conditions. (a)  $T_t$  in XY plane; (b)  $T_t$  in ZX plane; (c)  $T_{ve}$  in XY plane; (d):  $T_{ve}$  in ZX plane.

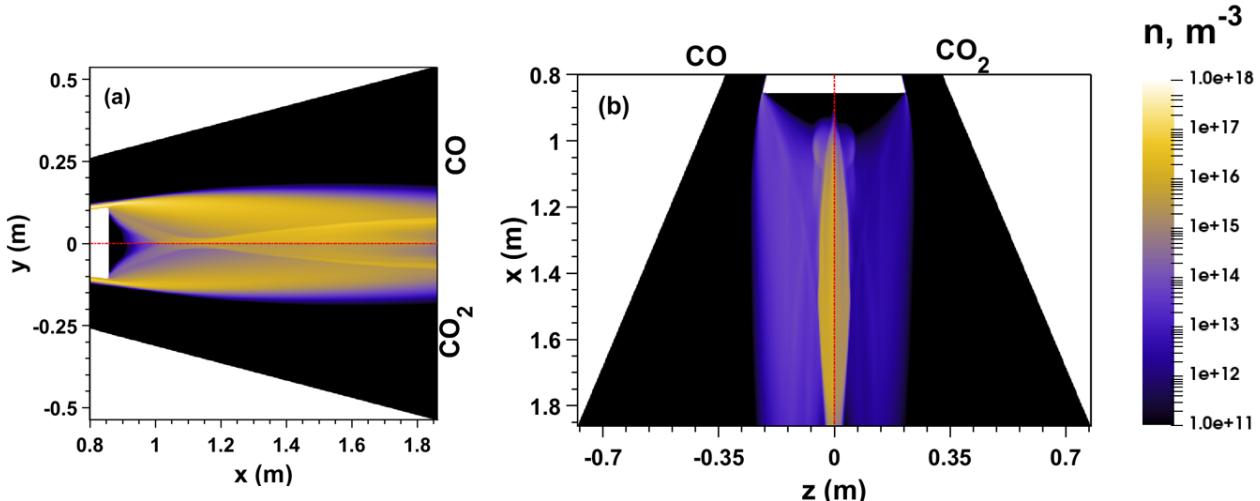
Figure 10 shows transverse slices of  $T_t$  and  $T_{ve}$  at planes located 0.50 m, and 0.75 m downstream of the vehicle base. Across both ablating and non-ablating conditions, only minor variations are observed in  $T_t$  and  $T_{ve}$  within each plane. In Figure 10a, early indications of a recirculating vortical thermal structure are evident, where the developing shear layer begins to roll over. Figure 10b shows 0.25 m downstream of Figure 10a, where this structure has matured, exhibiting a well-defined vortical structure with higher temperatures concentrated along the core of the vortices. In Figure 10c, further downstream, the vortical pattern persists but weakens, with the wake expanding and temperature gradients decreasing as the flow gradually approaches a more uniform state. Alongside these features, vibrational temperature exhibits a narrow, high  $T_{ve}$  stream near  $z = 0$ , remaining confined across planes. While the stream maintains its narrow shape, it gradually decreases its vertical extent downstream, also shown in Figure 9. By 0.75 m from the vehicle base, regions of elevated  $T_{ve}$  appear to only follow the contour of the wake shock, also shown in Figure 9.



**Fig. 10** Transverse temperature profiles in the wake under non-ablating (upper half,  $y > 0$ ) and ablating (lower half,  $y < 0$ ) conditions. Panels (a-c) show  $T_t$ , panels (d-f) show  $T_{ve}$ . Panel (a) shows early shear layer deformation; Panel (b) shows fully developed shear layer roll-over

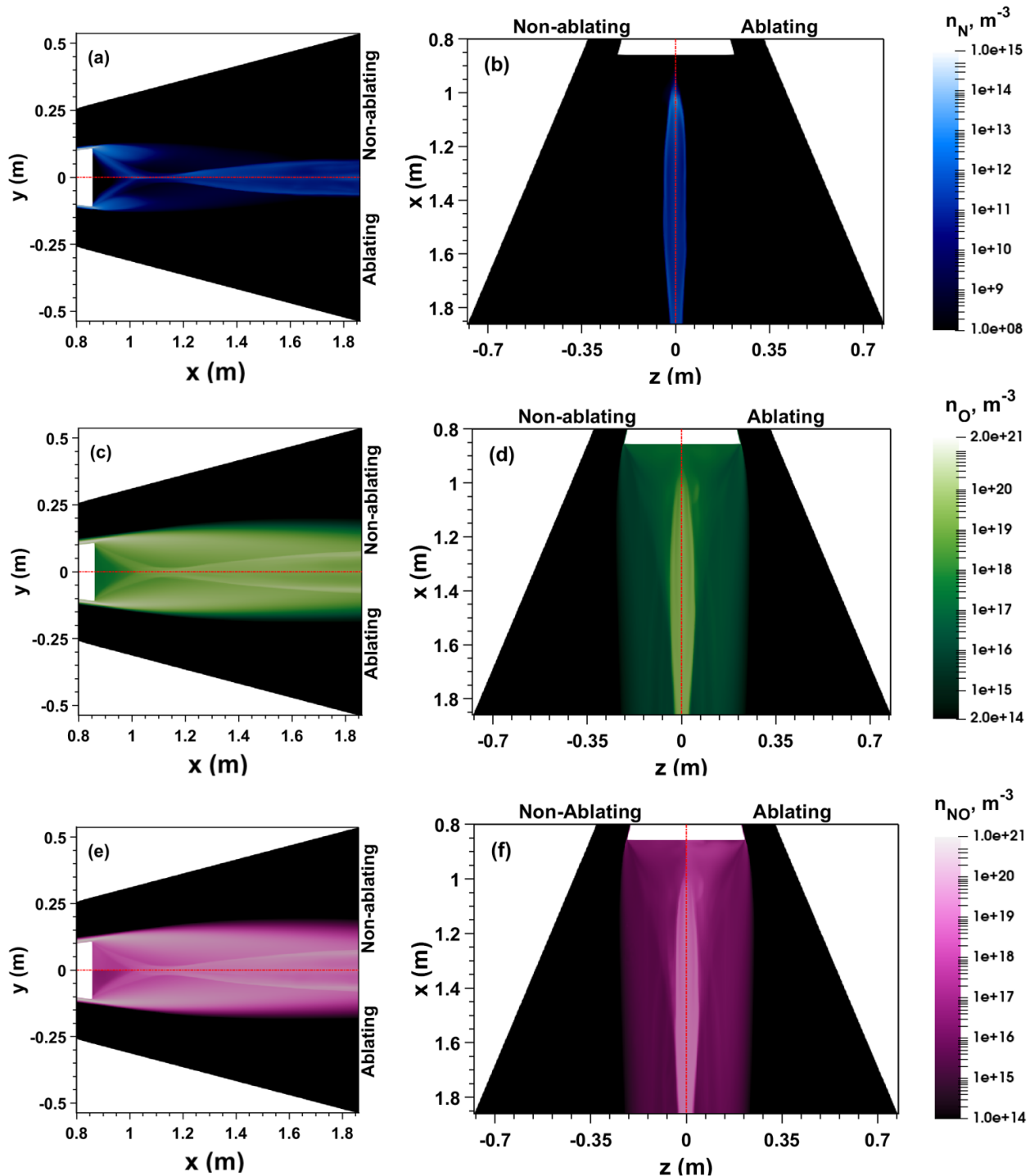
### C. Chemical composition of the wake

Figure 11 shows computed number density of carbon dioxide ( $\text{CO}_2$ ) and carbon monoxide (CO) in the wake.  $\text{CO}_2$  has strong emission features in the infrared region [6, 7], whereas CO has various emission features spanning the near-ultraviolet to visible to near-infrared regions [8–10]. The wake contains more CO than  $\text{CO}_2$ , consistent with CO being the dominant oxidation product formed at carbon-composite surfaces [47–49]. The presence of  $\text{CO}_2$  at comparable number density arises from secondary oxidation of CO and continued mixing of oxygen-bearing species in the wake. Both CO and  $\text{CO}_2$  reach their highest number densities along boundaries of the separated flow and within the wake core. Chemistry within the expansion region of a hypersonic wake remain chemically frozen [22], allowing ablation products formed over the forebody to persist in this region. The high density gradient formed along the wake core boundary (Figure 8) allow species to accumulate along this interface.



**Fig. 11** Number density,  $\text{m}^{-3}$ , of CO and  $\text{CO}_2$  in the wake. (a) XY plane; (b) ZX plane

Figure 12 shows the computed number density of atomic nitrogen (N), atomic oxygen (O) and nitric oxide (NO) in the wake under ablating and non-ablating conditions. N and O radiate distinct lines relevant to spectral analysis [22, 72] and rapidly recombine into their molecular forms in the wake, contributing to emissions from the  $\text{N}_2$  Lewis-Rayleigh afterglow [11] and  $\text{O}_2$  atmospheric and Herzberg (I,II) systems [11]. Several bands of NO excited state emission exist, extending from the mid-ultraviolet into the visible range [11, 73]. Little change in number density of N, O and NO can be seen in the wake for ablating and non-ablating conditions, suggesting that the ablation rates were again insufficient to warrant any change in species distributions. Similarly to CO and  $\text{CO}_2$ , N, O and NO can be found at high number density within the expansion region developed in the XY plane and throughout the wake core. Slightly more NO can be seen within the ZX plane of the wake, particularly within the recirculation region. As mentioned in Section IV.A, the production of NO under ablating conditions may be increased through reactions 9, 11 and 13 from Table 2. Chemistry remains largely frozen in the expansion region developed by a hypersonic wake [22], consequently NO in the near-wake is not as efficiently consumed or converted.



**Fig. 12** Planar views of number density,  $\text{m}^{-3}$ , of key air species in the wake under ablating and non-ablating conditions. (a-b) Atomic Nitrogen (N); (c-d) Atomic Oxygen (O); (e-f) Nitric Oxide (NO)

## V. Conclusions

Numerical simulations of the spatial distributions of radiating species and temperature in the wake generated by an ablating and non-ablating hypersonic glide vehicle were compared and analyzed. Ablation is found to increase nitric oxide production over the forebody relative to a non-ablating vehicle, allowing more nitric oxide to enter the wake. Carbon monoxide and carbon dioxide are identified as the major ablation products, persisting at notable levels throughout the wake. The developed wake exhibits two apparent neck positions due to crossflow established over the forebody, which produce localized peaks in translational and vibro-electronic temperatures. Despite these features, ablation has negligible influence on the overall wake flow structure at the flight conditions considered. The present results may inform analyses of radiative signatures and the interpretation of optical measurements in the wake of a hypersonic glide vehicle.

## Acknowledgments

The authors acknowledge support from the University of South Australia (UniSA), the University of Southern Queensland (UniSQ), iLAuNCH, the Australian Government Research Training Program Scholarship (RTPS) and the National Computational Infrastructure (NCI), an NCRIS enabled capability supported by the Australian Government.

## References

- [1] Steg, L., and Lew, H., "Hypersonic Ablation," Tech. rep., Space Sciences Laboratory, 1962. Report no. R62SD55.
- [2] White, T., Hwang, H., Ellerby, D., Gasch, M., Beck, R., Kam, J., and Venkatapathy, E., "Thermal Protection System Materials for Sample Return Missions," *Planetary Science Decadal Community White Papers*, 2020.
- [3] Taylor, R., B.W. Melcher II, and Washburn, W., "Studies of the luminous hypersonic wake," *AIAA Journal*, Vol. 2, No. 10, 1964. <https://doi.org/10.2514/3.2656>.
- [4] Stephenson, J., "Measurement of optical radiation from the wake of ablating blunt bodies in flight at speeds up to 10 km per second," NASA Technical Note, TN D-2760, 1965.
- [5] Craig, R., and Davey, W., "Thermal Radiation from Ablation Products Injected into a Hypersonic Shock Layer," Tech. rep., National Aeronautics and Space Administration, 1963. NASA Technical Note D-1978.
- [6] Mahulikar, S. P., Sonawane, H. R., and Rao, G. A., "Infrared signature studies of aerospace vehicles," *Progress in Aerospace Sciences*, Vol. 43, 2007. <https://doi.org/10.1016/j.paerosci.2007.06.002>.
- [7] Depraz, S., Perrin, M. Y., Riviere, P., and Soufiani, A., "Infrared emission spectroscopy of CO<sub>2</sub> at high temperature. Part II: Experimental results and comparisons with spectroscopic databases," *Journal of Quantitative Spectroscopy and Radiative Transfer*, Vol. 43, 2012. <https://doi.org/10.1016/j.jqsrt.2011.09.013>.
- [8] Wallace, L., "Band-Head Wavelengths of C<sub>2</sub>, CH, CN, CO, NH, NO, O<sub>2</sub>, OH and Their Ions," *Astrophysical Journal Supplement*, Vol. 7, 1962. <https://doi.org/10.1086/190078>.
- [9] Babou, Y., Riviere, P., Perrin, M.-Y., and Soufiani, A., "Spectroscopic data for the prediction of radiative transfer in CO<sub>2</sub>-N<sub>2</sub> plasmas," *Journal of Quantitative Spectroscopy and Radiative Transfer*, Vol. 110, 2009. <https://doi.org/10.1016/j.jqsrt.2008.09.007>.
- [10] Ferreira, R. G., Carvalho, B. B., Alves, L. L., Gonçalves, B., Villace, V. F., Marraffa, L., and da Silva, M. L., "VUV to IR Emission Spectroscopy and Interferometry Diagnostics for the European Shock Tube for High-Enthalpy Research," *Sensors*, Vol. 23, No. 13, 2023. <https://doi.org/10.3390/s23136027>.
- [11] Hundley, R., "Air Radiation From Nonequilibrium Wakes of Blunt Hypersonic Reentry Vehicles," RAND Memorandum,, 1964.
- [12] Daumont, D., Brion, J., Charbonnier, J., and Malicet, J., "Ozone UV spectroscopy I: Absorption cross-sections at room temperature," *Journal of Atmospheric Chemistry*, Vol. 15, 1992. <https://doi.org/10.1007/BF00053756>.
- [13] Malicet, J., Daumont, D., Charbonnier, J., Parisse, C., Chakir, A., and Brion, J., "Ozone UV spectroscopy. II. Absorption cross-sections and temperature dependence," *Journal of Atmospheric Chemistry*, Vol. 21, 1995. <https://doi.org/10.1007/BF00696758>.
- [14] Zhong, J., Ozawa, T., and Levin, D., "Comparison of High-Altitude Hypersonic Wake Flows of Slender and Blunt Bodies," *AIAA Journal*, Vol. 46, No. 1, 2008. <https://doi.org/10.2514/1.31056>.
- [15] Schwing, A., and Candler, G., "Detached-Eddy Simulation of Capsule Wake Flows and Comparison to Wind-Tunnel Test Data," *Journal of Spacecraft and Rockets*, Vol. 52, No. 2, 2015. <https://doi.org/10.2514/1.A32834>.
- [16] Hruschka, R., O'Byrne, S., and Kleine, H., "Comparison of velocity and temperature measurements with simulations in a hypersonic wake flow," *Experiments in Fluids*, Vol. 51, No. 2, 2011. <https://doi.org/10.1007/s00348-011-1039-9>.
- [17] Muramoto, K. K., "Model for Predicting Hypersonic Laminar Near-Wake Flowfields," *Journal of Spacecraft and Rockets*, Vol. 33, No. 2, 1996.
- [18] Lees, L., "Hypersonic Wakes and Trails," *AIAA Journal*, Vol. 2, No. 3, 1964. <https://doi.org/10.2514/3.2356>.
- [19] Sinha, K., Barnhardt, M., and Candler, G., "Detached Eddy Simulation of Hypersonic Base Flows with Application to Fire II Experiments," *AIAA Paper 2004-2633*, 2004. <https://doi.org/10.2514/6.2004-2633>.

- [20] Chang, P. K., *Separation of Flow*, Elsevier, 1970.
- [21] Tracy, C. L., and Wright, D., “Modeling the Performance of Hypersonic Boost-Glide Missiles,” *Science & Global Security*, Vol. 28, No. 3, 2020. <https://doi.org/10.1080/08929882.2020.1864945>.
- [22] Park, C., *Nonequilibrium Hypersonic Aerothermodynamics*, John Wiley Sons: Hoboken, NJ, USA, 1990.
- [23] Langan, W., Cresswell, J., and Browne, W., “Effects of Ablation Products on Ionization in Hypersonic Wakes,” *AIAA Journal*, Vol. 3, No. 12, 1965. <https://doi.org/10.2514/3.3348>.
- [24] Johnston, C., Gnoffo, P., and Mazaheri, A., “Influence of Coupled Radiation and Ablation on the Aerothermodynamic Environment of Planetary Entry Vehicles,” 2013.
- [25] Johnston, C., “Study of Aerothermodynamic Modeling Issues Relevant to High-Speed Sample Return Vehicles,” 2014.
- [26] Johnston, C. O., Brandis, A. M., and Sutton, K., “Shock Layer Radiation Modeling and Uncertainty for Mars Entry,” *AIAA Paper 2012-2866*, 2012. <https://doi.org/10.2514/6.2012-2866>.
- [27] Scoggins, J. B., Soucasse, L., Riviere, P., Soufiani, A., and Magin, T., “Coupled flow, radiation, and ablation simulations of atmospheric entry vehicles using the hybrid statistical narrow band model,” *AIAA Paper 2015-3112*, 2015. <https://doi.org/10.2514/6.2015-3112>.
- [28] Han, L., and Han, Y., “Effect of surface ablation on aerodynamic heating over a blunt cone in hypersonic airflow,” *Physics of Fluids*, Vol. 36, No. 3, 2024. <https://doi.org/10.1063/5.0196415>.
- [29] Gnoffo, P., Johnston, C., and Thompson, R., “Implementation of Radiation, Ablation, and Free Energy Minimization in Hypersonic Simulations,” *Journal of Spacecraft and Rockets*, Vol. 47, No. 2, 2010. <https://doi.org/10.2514/1.44916>.
- [30] Erb, A., West, T., and Johnston, C., “Investigation of Galileo Probe Entry Heating with Coupled Radiation and Ablation,” *Journal of Spacecraft and Rockets*, Vol. 57, No. 4, 2019. <https://doi.org/10.2514/1.A34751>.
- [31] Satchell, M. J., Layng, J. M., and Greendyke, R. B., “Numerical Simulation of Heat Transfer and Chemistry in the Wake behind a Hypersonic Slender Body at Angle of Attack,” *Aerospace*, Vol. 5, No. 1, 2018. <https://doi.org/10.3390/aerospace5010030>.
- [32] Bartlett, E., Anderson, L., and Curry, D., “An evaluation of Ablation Mechanisms for the Apollo Heat Shield Material,” *Journal of Spacecraft and Rockets*, Vol. 8, No. 5, 1971. <https://doi.org/10.2514/3.59679>.
- [33] Walker, S., Sherk, J., Shell, D., Schena, R., Bergmann, J., and Gladbach, J., “The DARPA/AF Falcon Program: The Hypersonic Technology Vehicle 2 (HTV-2) Flight Demonstration Phase,” *AIAA Paper 2008-2539*, 2008. <https://doi.org/10.2514/6.2008-2539>.
- [34] Kimmel, R., Adamczak, D., D.Hartley, Alesi, H., Frost, M., Pietsch, R., J.Shannon, and Silvester, T., “Hypersonic International Flight Research Experimentation-5b Flight Overview,” *Spacecraft and Rockets*, Vol. 55, No. 6, 2018. <https://doi.org/10.2514/1.A34148>.
- [35] “Github repository of the hyStrath platform,” <https://github.com/hystrath/hyStrath/>, 2022. Release 1.0, commit 984e300.
- [36] Casseau, V., Espinoza, D. E., Scanlon, T. J., and Brown, R. E., “A Two-Temperature Open-Source CFD Model for Hypersonic Reacting Flows, Part Two: Multi-Dimensional Analysis,” *Aerospace*, Vol. 3, No. 4, 2016. <https://doi.org/10.3390/aerospace3040045>.
- [37] Casseau, V., Palharini, R. C., Scanlon, T. J., and Brown, R. E., “A Two-Temperature Open-Source CFD Model for Hypersonic Reacting Flows, Part One: Zero-Dimensional Analysis,” *Aerospace*, Vol. 3, No. 4, 2016. <https://doi.org/10.3390/aerospace3040034>.
- [38] Wright, M. J., Bose, D., Palmer, G., and Levin, E., “Recommended Collision Integrals for Transport Property Computations Part 1: Air Species,” *AIAA Journal*, Vol. 43, No. 12, 2005. <https://doi.org/10.2514/1.16713>.
- [39] Wright, M. J., Hwang, H. H., and Schwenke, D. W., “Recommended Collision Integrals for Transport Property Computations Part 2: Mars and Venus Entries,” *AIAA Journal*, Vol. 45, No. 1, 2007. <https://doi.org/10.2514/1.24523>.
- [40] Park, C., “Review of Chemical-Kinetic Problems of Future NASA missions, I: Earth Entries,” *Journal of Thermophysics and Heat Transfer*, Vol. 7, No. 3, 1993. <https://doi.org/10.2514/3.431>.

- [41] Fujita, K., Yamada, T., and Ishii, N., "Impacts of Ablation Gas Kinetics on Hyperbolic Entry Radiative Heating," *AIAA Paper 2006-1185*, 2012. <https://doi.org/10.2514/6.2006-1185>.
- [42] C.Park, Howe, J., Jaffe, R., and Candler, G., "Review of Chemical-Kinetic Problems of Future NASA Missions, II: Mars Entries," *Journal of Thermophysics and Heat Transfer*, Vol. 8, No. 1, 1994. <https://doi.org/10.2514/3.496>.
- [43] Gokcen, T., "N<sub>2</sub>-CH<sub>4</sub>-Ar Chemical Kinetic Model for Simulations of Atmospheric Entry to Titan," *Journal of Thermophysics and Heat Transfer*, Vol. 21, No. 1, 2007. <https://doi.org/10.2514/1.22095>.
- [44] Scalabrin, L., "Numerical Simulation of Weakly Ionized Hypersonic Flow over Reentry Capsules," Ph.D. thesis, University of Michigan, Ann Arbor (US), 2007.
- [45] Metzger, J. W., Engel, M. J., and Diaconis, N. S., "Oxidation and Sublimation of Graphite in Simulated Re-Entry Environments," *AIAA Journal*, Vol. 5, No. 3, 1967. <https://doi.org/10.2514/3.4001>.
- [46] Scala, S. M., and Gilbert, L. M., "Sublimation of Graphite at Hypersonic Speeds," *AIAA Journal*, Vol. 3, No. 9, 1965. <https://doi.org/10.2514/3.3220>.
- [47] Liu, G., "High Temperature Oxidation of Graphite by a Dissociated Oxygen Beam," Ph.D. thesis, Dept. of Aeronautics and Astronautics, Massachusetts Inst. of Technology, Cambridge, 1973.
- [48] Park, C., Jaffe, R., and Partridge, H., "Chemical-Kinetic Parameters of Hyperbolic Earth Entry," *Journal of Thermophysics and Heat Transfer*, Vol. 15, No. 1, 2001. <https://doi.org/10.2514/2.6582>.
- [49] Keenan, J., and Candler, G., "Nonequilibrium Processes in Hypervelocity Flows: An Analysis of Carbon Ablation Models," *AIAA Paper 2012-0724*, 2012. <https://doi.org/10.2514/6.2012-724>.
- [50] Driver, D., and MacLean, M., "Improved Predictions of PICA Recession in Arc Jet Shear Tests," *AIAA Paper 2011-0141*, 2011. <https://doi.org/10.2514/6.2011-141>.
- [51] Lachaud, J., and Mansour, N., "Porous-Material Analysis Toolbox Based on OpenFOAM and Applications," *Journal of Thermophysics and Heat Transfer*, Vol. 28, No. 2, 2014. <https://doi.org/10.2514/1.T4262>.
- [52] Wang, Y., Chatterjee, P., and de Ris, J. L., "Large eddy simulation of fire plumes," *Proceedings of the Combustion Institute*, Vol. 33, No. 2, 2011. <https://doi.org/10.1016/j.proci.2010.07.031>.
- [53] Trouve, A., and Wang, Y., "Large eddy simulation of compartment fires," *International Journal of Computational Fluid Dynamics*, Vol. 24, No. 10, 2010. <https://doi.org/10.1080/10618562.2010.541393>.
- [54] Grange, N., Chetehouna, K., Gascouin, N., Coppalle, A., Reynaud, I., and Senave, S., "One-dimensional pyrolysis of carbon based composite materials using FireFOAM," *Fire Safety Journal*, Vol. 97, 2018. <https://doi.org/10.1016/j.firesaf.2018.03.002>.
- [55] Chen, Y. K., and Milos, F. S., "Ablation and Thermal Response Program for Spacecraft Heatshield Analysis," *Journal of Spacecraft and Rockets*, Vol. 36, No. 3, 1999. <https://doi.org/10.2514/2.3469>.
- [56] Dimitrienko, Y. I., *Thermomechanics of composites under high temperatures*, Vol. 65, Springer Science & Business Media, 2013.
- [57] Kianvashrad, N., and Knight, D., "Nonequilibrium Effects on Prediction of Aerothermodynamic Loading for a Double Cone," *AIAA Journal*, Vol. 57, No. 7, 2019. <https://doi.org/10.2514/1.J057883>.
- [58] Kieweg, S., Ray, J., Weirs, V., Carnes, B., Dinzl, D., Freno, B., Howard, M., Phipps, E., Rider, W., and Smith, T., "Validation Assessment of Hypersonic Double-Cone Flow Simulations using Uncertainty Quantification, Sensitivity Analysis, and Validation Metrics," *AIAA SciTech 2019 Forum*, edited by Americain Institute of Aeronautics and Astronautics, 2019.
- [59] Knight, D., Longo, J., Drikakis, D., Gaitonde, D., Lani, A., Nompelis, I., Reimann, B., and Walpot, L., "Assessment of CFD capability for prediction of hypersonic shock interactions," *Progress in Aerospace Sciences*, Vol. 48-49, 2012. <https://doi.org/10.1016/j.paerosci.2011.10.001>.
- [60] Juliano, T. J., Jewell, J. S., and Kimmel, R. L., "Effects of Attitude on HIFiRE-5b Boundary-Layer Transition," *Journal of Spacecraft and Rockets*, Vol. 56, No. 4, 2019. <https://doi.org/10.2514/1.A34352>.
- [61] Juliano, T., Poggie, J., Porter, M., Kimmel, R., Jewell, J., and Adamczak, D., "HIFiRE-5b Heat Flux and Boundary-Layer Transition," *Spacecraft and Rockets*, Vol. 55, No. 6, 2018. <https://doi.org/10.2514/1.A34147>.

- [62] Juliano, T., Jewell, J., and Kimmel, R., "HIFiRE-5b Boundary-Layer Transition — with Attitude," *AIAA Paper 2018–2891*, 2018. <https://doi.org/10.2514/6.2018-2891>.
- [63] Juliano, T., Jewell, J., and Kimmel, R., "HIFiRE-5b Boundary-Layer Transition Length and Turbulent Overshoot," *Journal of Spacecraft and Rockets*, Vol. 58, No. 2, 2021. <https://doi.org/10.2514/1.A34856>.
- [64] Kimmel, R. L., Adamczak, D., Berger, K., and Choudari, M., "HIFiRE-5 Flight Vehicle Design," *AIAA Paper 2010–4985*, 2010. <https://doi.org/10.2514/6.2010-4985>.
- [65] Urzay, J., "General Velocity-Altitude Flight-Regime Diagram for Aeronautics and Astronautics," *Journal of Spacecraft and Rockets*, Vol. 62, No. 2, 2024. <https://doi.org/10.2514/1.A36169>.
- [66] Levensteins, Z., and Krumins, M., "Aerodynamic Characteristics of Hypersonic Wakes," *AIAA Journal*, Vol. 5, No. 9, 1967. <https://doi.org/10.2514/3.4256>.
- [67] Jr., H. Q., Paredes, P., Hanifi, A., and Theofilis, V., "Transient growth analysis of hypersonic flow over an elliptic cone," *Journal of Fluid Mechanics*, Vol. 935, 2022. <https://doi.org/10.1017/jfm.2022.46>.
- [68] Huntley, M., and Smits, A., "Transition studies on an elliptic cone in Mach 8 flow using Filtered Rayleigh Scattering," *European Journal of Mechanics - B/Fluids*, Vol. 19, No. 5, 2000. [https://doi.org/10.1016/S0997-7546\(00\)00130-8](https://doi.org/10.1016/S0997-7546(00)00130-8).
- [69] Tufts, M., Borg, M., Bisek, N., and Kimmel, R., "High-Fidelity Simulation of HIFiRE-5 Boundary-Layer Transition," *AIAA Journal*, Vol. 4, No. 60, 2022. <https://doi.org/10.2514/1.J060090>.
- [70] Gosse, R., Kimmel, R., and Johnson, H., "CFD Study of the HIFiRE-5 Flight Experiment," *AIAA Paper 2010–4854*, 2010. <https://doi.org/10.2514/6.2010-4854>.
- [71] Li, F., Choudhari, M., Chang, C.-L., and White, J., "Stability Analysis for HIFiRE Experiments," *AIAA Paper 2012–2961*, 2010. <https://doi.org/10.2514/6.2012-2961>.
- [72] Dorrance, W., *Viscous Hypersonic Flow: Theory of Reacting and Hypersonic Boundary Layers*, Courier Dover Publications, 2017.
- [73] Gorshkov, A., "The simulation of ultraviolet radiation under conditions of re-entry of space vehicle from near-earth orbit," *High Temperature*, Vol. 48, 2010. <https://doi.org/10.1134/S0018151X10010037>.